Additive Manufacturing 118 (2026) 105108

Contents lists available at ScienceDirect

Additive Manufacturing

journal homepage: www.elsevier.com/locate/addma

Research paper

Printing force analysis in FDM-based 4D printing of singular lines: A numerical and experimental study

Ferdinand Cerbe [a,*,1], Felipe A. González [b,c,1], Michael Sinapius [a], Marek Behr [b,c], Stefanie Elgeti [d]

[a] Institute of Mechanics and Adaptronics, TU Braunschweig, Langer Kamp 6, Braunschweig, 38106, Germany
[b] Chair for Computational Analysis of Technical Systems (CATS), RWTH Aachen University, Schinkelstraße 2, Aachen, 52062, Germany
[c] Center for Simulation and Data Science (JARA-CSD), RWTH Aachen University, Schinkelstraße 2, Aachen, 52062, Germany
[d] Institute of Lightweight Design and Structural Biomechanics (ILSB), TU Wien, Gumpendorfer Straße 7, Vienna, A-1060, Austria

ARTICLE INFO

Keywords:
Fused deposition modeling (FDM)
4D printing
Printing force analysis
Shape memory polymers
Computational fluid dynamics (CFD)

ABSTRACT

Fused deposition modeling (FDM)-based 4D printing (4DP) provides a low-cost pathway to fabricate programmable structures, but its broader adoption is limited by an incomplete understanding of how process conditions affect internal stress development and resulting shape change. Building on prior work linking 4DP to the shape-memory cycle, this study investigates how process parameters influence the flow and temperature fields during the deposition of a singular line. Printing force is measured in situ and compared with wall shear force from a high-fidelity thermofluid simulation. The numerical framework is calibrated using infrared thermography and a Cross–Williams–Landel–Ferry (Cross-WLF) viscosity model for polylactic acid (PLA). Sensitivity analysis identifies gap height, nozzle temperature, and volumetric flow rate as the dominant parameters governing the printing force, while printing speed serves as an effective design variable for manipulating the printing force continuously. The simulations further show that shear rates are concentrated at the nozzle exit and the deposition front, explaining heterogeneous pre-strain across the filament cross-section. Experimental and numerical trends are consistent: increasing nozzle temperature reduces the printing force, while increasing printing speed increases it. This combined experimental–numerical approach provides a methodology to improve process control by analyzing flow conditions during smart structure manufacturing.

1. Introduction

4D printing (4DP) is an emerging technology that allows the **Additive manufacturing (AM)** of objects that change their characteristics over time, by utilizing smart materials in AM [1–3]. The change mechanism is activated by a so-called stimulus, such as temperature [4,5], ultraviolet radiation [6,7], magnetism [8], infrared radiation [9], or moisture [10]. The characteristic change can be a shape or color change, or an energy conversion from deformation energy to electrical energy [11] and vice versa [12]. Additionally, several AM processes have been used to manufacture 4D objects [2]. The adaptability and versatile complex behavior of 4DP, particularly its ability to achieve unique shape-changing behaviors, make it highly suitable for applications in robotics [13], aerospace structures [14], metamaterial [15,16], and biomedical engineering such as drug delivery, orthopedics, medical devices, tissue engineering, and dentistry [17]. However, current challenges are the controllability of the 4D object and understanding the fundamental mechanisms.

4DP with the AM process **Fused deposition modeling (FDM)** is a promising technology, due to the cost-efficient materials and printers [3]. Here, **Shape memory polymers (SMP)** or thermo-sensitive polymers with a sharp glass transition, such as **polylactic acid (PLA)**, are programmed during printing [18] or after printing [19] and change their shape when they are activated thermally by heating the structure above a transition temperature [17]. The shape change utilizes the process-inherent anisotropy and mainly occurs in the printing direction [18,20], where the highest residual stress is induced. On a molecular level, the extrusion and deposition orient the polymer chains, and fast cooling freezes the residual stress as a pre-strain. This pre-strain can also be used to design more complex shape changes, such as bending, twisting, and combinations [21] by changing printing

* Corresponding author.
E-mail addresses: f.cerbe@tu-braunschweig.de (F. Cerbe), gonzalez@cats.rwth-aachen.de (F.A. González), m.sinapius@tu-braunschweig.de (M. Sinapius), behr@cats.rwth-aachen.de (M. Behr), elgeti@ilsb.tuwien.ac.at (S. Elgeti).
[1] These authors contributed equally to this work.

https://doi.org/10.1016/j.addma.2026.105108
Received 18 November 2025; Received in revised form 15 January 2026; Accepted 31 January 2026
Available online 2 February 2026

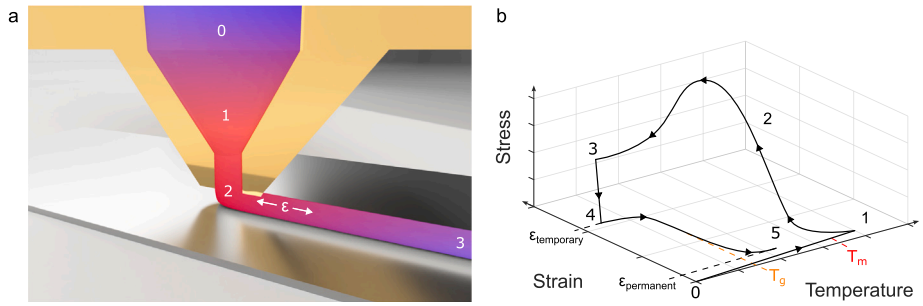

Fig. 1. The hypothetical temperature and strain in 4DP (a) and the respective shape memory cycle (b). During printing, the cold material is fed to the nozzle (0) and melted by raising its temperature above T_m (1). The material is programmed during extrusion and deposition, where it is stretched and cools down (2) until the shape is fixed (3). After printing, the part is removed from the build plate and stays in its temporary shape (4). When heated above T_g, it recovers its permanent shape (5).

direction and the amount of shrinkage, which depends on printing parameters, such as nozzle temperature, printing speed, and layer height.

Although a comparison of the quantitative shrinkage of different 4DP studies is difficult due to different printers, materials, and object geometries, the general effects of printing parameters on shape transformation are consistent. Decreasing the nozzle temperature [20,22–24], increasing printing speed [21,25–28], and decreasing layer height [20,24,29–31] increase shape transformation. Decreasing the nozzle temperature increases the relaxation time and allows better fixation of the manufacturing-induced pre-strain. Increasing printing speed and decreasing layer height both cause a higher shear rate, which induces more pre-strain, leading to a larger shape transformation [32]. Therefore, the qualitative trends are consistent with polymer rheology. However, the main challenge is to accurately predict the pre-strain with respect to the printing parameters, so the shape change occurs as desired [32]. Even though the 4DP technology has significantly evolved, numerical studies are restricted to the transformation dynamics of smart structures, sometimes including viscoelastic models [3,19,21,33,34]. There has been the ambition to use statistical models for pre-strain prediction, and they were shown to be useful for parameter optimization on a specific 3D printer [35], but these models are not based on physical phenomena or differential equations. Regarding the manufacturing process, simulations are limited to 3D printing only [36,37]. The transformation simulations easily consider multiple lines and layers to predict and design different shape changes. However, a high-fidelity manufacturing simulation of the deposition process of a multi-layer smart structure is costly. Therefore, manufacturing simulations are often limited to a few lines and layers only [36–38]. In 4DP, the singular line is the driving element of the transformation of a structure, which makes it particularly interesting to study experimentally and numerically. Although printing of subsequent lines and layers causes reheating, relaxation, and ultimately affects the final pre-strain, understanding the state of a singular line after deposition is an important first step to improve process control. Therefore, we focus on the deposition of a singular 4D printed line in this article and investigate it using experimental and numerical methods to determine its temperature evolution and the force in the printing direction.

In an earlier work, one of the current authors presents a method to determine the stresses when 4D printing a smart structure [32]. In this study, force measurement was integrated into the printing process to analyze the programming force. Because the measured force represents a superposition of programming, friction, and viscous components, the term programming force is misleading and must be interpreted as a printing force. Nevertheless, it constitutes a step towards linking the well-established shape memory cycle to 4DP. The shape memory cycle is a standardized procedure used to evaluate whether an SMP can be programmed into a temporary shape and subsequently recover its original form upon reheating [39,40]. It is characterized by the parameters stress, strain, temperature, and time, where the stress–strain relationship is strongly temperature-dependent. As shown in Fig. 1, the printing process can be linked to the hypothetical shape memory cycle. However, the strain in 4DP cannot be measured directly. Therefore, the progression in Fig. 1(b) is only hypothetical. To achieve further insight, Cerbe et al. used the recovered strain on activation and the force measurements during printing to determine the relationship between printing stress and recovered strain [32]. Note that the printing stress is only an accessible process-level indicator of flow resistance and deformation during deposition. However, it also shares a relationship with the recovered strain in the particular study. Cerbe et al. further demonstrated that this relationship is not unique for a material but depends on its thermal history. These findings highlight the need for additional sensing to record the temperature history and to utilize high-fidelity flow simulations to improve process understanding.

Numerical models have been developed to capture polymer behavior across the entire FDM process, including liquefication, extrusion, deposition, cooling, and solidification [37]. Given the complexity of the process, modeling is typically divided into three stages: liquefier and nozzle dynamics, extrusion and deposition, and final piece formation. Each stage contributes to the pressure, velocity, and temperature fields, consequently affecting the thermo-fluid behavior.

In the liquefier and nozzle stage, the material is subjected to high shear rates, particularly near the nozzle walls [41,42]. These shear conditions promote an axisymmetric polymer chain alignment and disentanglement, thereby driving them away from their equilibrium state [41]. According to Rouse relaxation and reptation theories, decreasing temperature increases relaxation times, which raises the Weissenberg number and enhances deviations from the equilibrium state.

During extrusion and deposition, the molten polymer cools through convective heat transfer to the surrounding air before contacting the build plate. Once it touches the build plate, conductive heat transfer becomes dominant, further accelerating the cooling process. The fast cooling prevents the formation of crystalline regions, resulting in a final part with a low crystallinity of 1.45% [43], and its effect on the material properties can be considered negligible. The main challenges in modeling this stage are the large surface deformations and the high thermal gradients of the polymer melt. These deformations generate non-uniform residual stresses and asymmetric polymer chain orientations over the line's height [44]. It also complicates capturing the evolution of the free surface of individual strands, which directly affects porosity and ultimately the mechanical and shape-changing properties of the printed part [37].

The evolution of strand surfaces during deposition is typically modeled using either two-phase or single-phase flow approaches. Two-phase models explicitly account for both the polymer melt and the surrounding air, and the accuracy of the strand shape is given by the mesh size at the interface [38,45–47]. Such an approach can become numerically expensive in three-dimensional simulations, especially when high accuracy of the strand shape is required. In contrast,

by neglecting the effect of the surrounding air, single-phase models consider only the polymer domain, which reduces computational cost but introduces challenges in tracking the highly deformable free surface. In this case, Lagrangian tracking requires robust mesh-handling strategies. Full remeshing methods are available in ANSYS Polyflow, and successfully used in strand deposition simulations [48,49]. However, full remeshing can also be computationally expensive, especially in three-dimensional simulations. In an earlier work, one of the current authors proposes a more efficient mesh-update technique [50,51]. This technique is based on a locally remeshing approach [52], with the key benefits of avoiding large-scale mesh generation and the inaccuracies introduced by mesh-to-mesh interpolation. Furthermore, it is designed to handle problems involving enlarging domains, making it particularly suitable for simulations like strand deposition.

The behavior of molten polymer during extrusion has recently been studied at different levels of complexity, ranging from Newtonian fluid models [38,45,53,54], to generalized Newtonian fluid (GNF) models [47,49,55–65], and viscoelastic fluid models [46,49,56]. These approaches include both isothermal [38,45,53,54,59] and non-isothermal formulations [46–49,55–58,60–65] based on the Arrhenius and Williams–Landel–Ferry (WLF) corrections. The isothermal Newtonian model assumes that the viscosity of the polymer melt does not affect strand shape [38]. However, both shear-thinning behavior and the strong temperature dependence of viscosity have a critical influence on the thermofluid behavior and, consequently, on the strand cross-section [61].

According to the literature, most researchers prefer the non-isothermal GNF model primarily due to two factors. First, the viscous model simplifies the modeling process and significantly reduces computational costs compared to the viscoelastic one. Second, the viscous model provides accurate predictions of the cross-section and better agreement with experimental results. Even though GNF models provide valuable insights, they cannot predict residual stresses [49]. In a recent numerical study, Lukhi et al. investigated residual stress formation using a viscoelastic Phan–Thien–Tanner (PTT) model and compared the results to a GNF formulation. While both models produced similar pressure distributions at the nozzle exit, the absence of a memory function in the GNF model led to pressure differences of up to five orders of magnitude. In contrast, the PTT model predicted residual stresses that gradually relaxed with time and distance from the nozzle [49]. Importantly, the simulations revealed a residual stress gradient, with higher values on the bottom side of the strand and lower values on the top side at a distance of 4 mm from the nozzle. This gradient is supported by their experimental observations, where printed strands exhibited downward bending towards the substrate upon activation. Although a direct quantitative comparison between simulation and experiment was not possible in their study, the implementation of viscoelastic models such as PTT appears highly promising for predicting residual stresses in 4DP. However, the pronounced die swell of the viscoelastic simulation was not observed in our experiments, showing that the viscoelastic behavior is not prominent during our strand deposition experiments.

Literature emphasizes that reliable flow simulations depend critically on three factors: the use of material models that adequately represent the materials' viscosity or viscoelasticity, the incorporation of accurate parameters, particularly for temperature evolution, and the availability of advanced numerical modeling techniques that allow for quantitative validation. Furthermore, advanced measurements must be used for verification to identify discrepancies and improve modeling approaches.

This study focuses on single-line deposition to isolate the flow phenomenon during deposition and use the printing force as a measurable process-level indicator of flow-induced pre-strain, and for comparison with the simulation. For this approach, we chose a combined experimental and numerical approach. Experimentally, we record the temperature history and printing force while fabricating singular 4D lines under varying nozzle temperatures and speeds. Oscillatory rheology is performed on PLA to characterize its temperature- and rate-dependent melt behavior, which is then used to calibrate a Cross-WLF viscosity model. After printing, the 4D lines are thermally activated in an oven to induce shape transformation. Numerically, the experimental rheology data and measured temperature history serve as inputs to calibrate the simulations. The purely viscous Cross-WLF model was chosen because it significantly reduces the computational complexity, provides accurate predictions of the extruded cross-sections, and our experiments did not show pronounced die swell. Moreover, the objective of this work is to assess whether such viscous models can also capture the printing forces and to identify potential improvements in material melt modeling. Furthermore, the simulation framework enables rapid variation of printing parameters (volumetric flow, gap height, and nozzle speed) to systematically quantify their influence on the printing force. While the experimental printing force is one indicator for manufacturing-induced pre-strain, the viscous simulation cannot capture the residual stress formation.

2. Materials and methods

2.1. Experimental investigations

The experimental studies focus on three values. First, the viscosity of the material is determined, and a cross-WLF model is calibrated with the data. This provides the viscosity model used in the simulation. Then, the temperature of the deposited material is measured with an infrared camera. The recorded temperature distribution helps to identify the heat transfer coefficients for the simulation. Finally, the forces that occur during printing are measured. These forces are then used in Section 3.3, where they are compared with the forces from the simulation.

2.1.1. Rheometry of PLA

The viscosity of PLA is measured with oscillation rheometry according to DIN EN ISO 3219-2:2021-08. The Anton Paar MCR702 is equipped with the HTD400, and the parallel plate system with 25 mm in diameter. The gap height during the experiments is 1.25 mm and the deformation is $\gamma = 1\%$, which is within the determined linear viscoelastic region. The experiments have been conducted for the angular frequencies from $\omega = 0.628$ to $\omega = 628$. The viscosities are determined for the temperatures 140 to 190 °C in 10 °C increments. The oscillation experiments consist of the following steps: loading the specimen at 100 °C (1). Heating to 160 °C and holding the temperature for 10 min (2). Trimming the sample with a hot trimming tool (3). Cooling the material to 140 °C and hold the temperature for 15 min (4). Measure the complex properties for $\omega = 0.628 - 628\ s^{-1}$ (5). Increase the temperature by the 10 °C, hold the temperature for 5 min and repeat step 5 (6).

The specimen was prepared using a scientific injection molding system (Thermo Fischer MiniJet) with a circular disc mold with a diameter of 25 mm. First, the filament material is granulated to a size < 4 mm. The material was not dried to mimic similar conditions as during the experiment with the 3D printer. The material is then loaded into the Minijet reservoir. The reservoir temperature is 200 °C. During preparation, the time is monitored. All specimens were prepared within 10 min after loading the reservoir. This was done to prevent thermal degradation, which would cause a decrease in PLA's viscosity [66].

The rheology of the material is shown in Fig. 2. The van Gurp–Palmen-plot in Fig. 2(a) shows, that the phase angle δ and the absolute value of the complex modulus $|G^*|$ follows the same curve progression for all temperatures. It shows that time–temperature superposition applies to this material in the presented temperature range [67].

An increasing temperature reduces the melt viscosity, see Fig. 2(b). Furthermore, the change due to shear rate decreases, see Fig. 2(c). It shows, that the PLA melt is a shear-thinning non-Newtonian fluid.

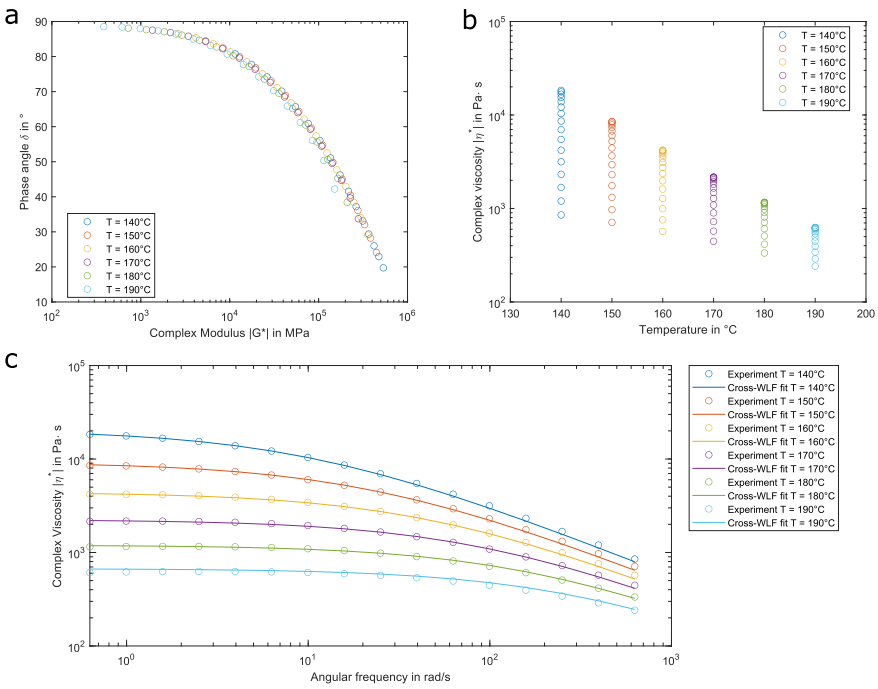

Fig. 2. Rheology results: in the van Gurp–Palmen-plot (a), viscosity-temperature plot (b), and the model to experiment comparison in the viscosity-angular frequency plot for different temperatures.

Table 1
Cross-WLF model parameters used in the simulation.

Parameter	Value
Critical stress at the shear thinning transition τ^*	2.0974×10^5 Pa
Power law index n	0.22
Zero viscosity at the reference temperature D_1	2.0531×10^4 Pa s
Reference temperature T_{ref}	140 °C
1st WLF coefficient A_1	18.67
2nd WLF coefficient A_2	222.8 °C

The results are interpreted with the assumption of the Cox–Merz relationship, so that $|\eta^*(\omega)| = \eta(\dot{\gamma})$[68]. The shear-thinning, temperature-dependent behavior can be approximated using the Cross-WLF-function (1). The material model was calibrated using a non-linear least-squares curve fitting procedure conducted in three steps. First, the power-law index (n), critical shear stress (τ^*), and zero-shear viscosity (η_0) were fitted independently for six temperatures, yielding shear rate-dependent functions for each case. Second, the parameters n and τ^* were averaged across all temperatures and fixed to their mean values. With these parameters held constant, η_0 was refitted for each temperature, exhibiting only minor deviations from the initial estimates. Finally, the temperature dependence of the zero-shear viscosity was characterized using the WLF equation, employing the zero-shear viscosity at the reference temperature ($D_1 = \eta_0(T = T_{\text{ref}})$) to determine the WLF coefficients A_1 and A_2. The resulting model parameters are presented in Table 1. The Cross-WLF model represents the melt's frequency- and temperature-dependent behavior well.

$$\eta(T, \dot{\gamma}) = \frac{\eta_0(T)}{1 + \left(\frac{\eta_0(T)}{\tau^*}\dot{\gamma}\right)^{1-n}}$$
$$\eta_0(T) = D_1 \cdot \exp\left(-\frac{A_1(T - T_{\text{ref}})}{A_2 + (T - T_{\text{ref}})}\right) \quad (1)$$

2.1.2. Temperature measurement during printing

The temperature is measured using a TIM VGA 640 infrared camera equipped with a microbolometer detector. The camera is positioned frontally to the printer, shown in Fig. 3(a), with the printing direction perpendicular to the line of sight, so that the deposited line crosses the image horizontally from right to left. The orientation reduces, but does not fully eliminate, angle-dependent errors introduced by the curved strand surface. The camera's temperature range is set to 0−250 °C, with a recording frequency of 125 Hz. At this frame rate, the resolution is limited to 640 × 120 pixels. The microscope lens provides a field of view of 12° ×9° with a focal length of 44 mm. The image scale is calibrated using a metal ruler, see Fig. 3(b), yielding a distance-to-pixel ratio of 22 mm over 640 px, corresponding to 0.0344 $\frac{\text{mm}}{\text{px}}$. The measurement accuracy is ±2 °C or ±2%, whichever is greater.

Emissivity is a critical parameter in IR temperature measurements, as it depends primarily on the material and surface characteristics. In theory, PLA has an emissivity of approximately 0.9, which is typical for many plastics [69]. However, the smooth, glossy surface of the melt during deposition reduces the effective emissivity. To calibrate emissivity for this specific setup, the melt temperature at the nozzle exit was approximated using a type-K thermocouple. Measurements showed that the nozzle tip temperature was approximately 37−39 °C lower than the set temperature in the slicer. The respective set nozzle temperature and the measured nozzle tip temperature are shown in Table 2. The IR camera's emissivity setting was then adjusted until the measured strand temperature matched the thermocouple reading, resulting in a calibrated value of $\epsilon = 0.675$. Using this method, the absolute temperature of the strand is slightly overestimated, however, the qualitative trend remains reliable. The printed line was recorded in an IR video, and sixteen rectangular measurement fields (2 × 20 pixels each) were evenly distributed along the line at intervals of 40 pixels, shown in Fig. 3(b). For each field, the maximum temperature was extracted over time, yielding a temperature–time curve that describes the temporal cooling behavior. To analyze the spatial temperature evolution, the frame in which the nozzle reached the leftmost field was used as a reference, enabling evaluation of the temperature distribution along the line at that moment. For statistical assurance, the experimental results in Fig. 6 represent the average and standard deviation of ten repeated prints.

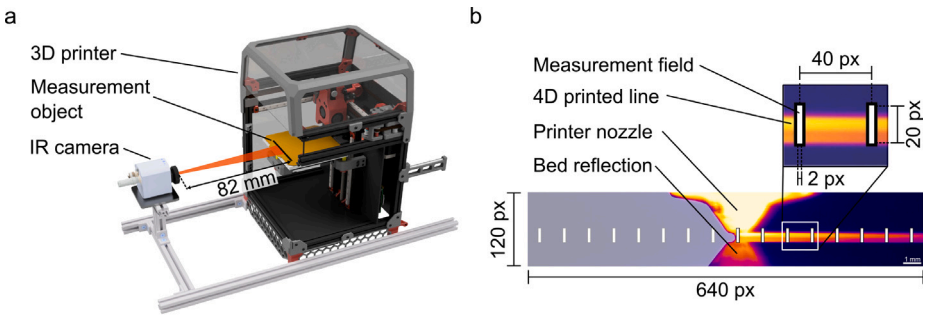

Fig. 3. Positioning the IR camera in front of the printer (a) allows for filming the printing of a line in a side view (b). The total width of the IR image spans a horizontal distance of 22 mm (1 px = 0.0344 mm).

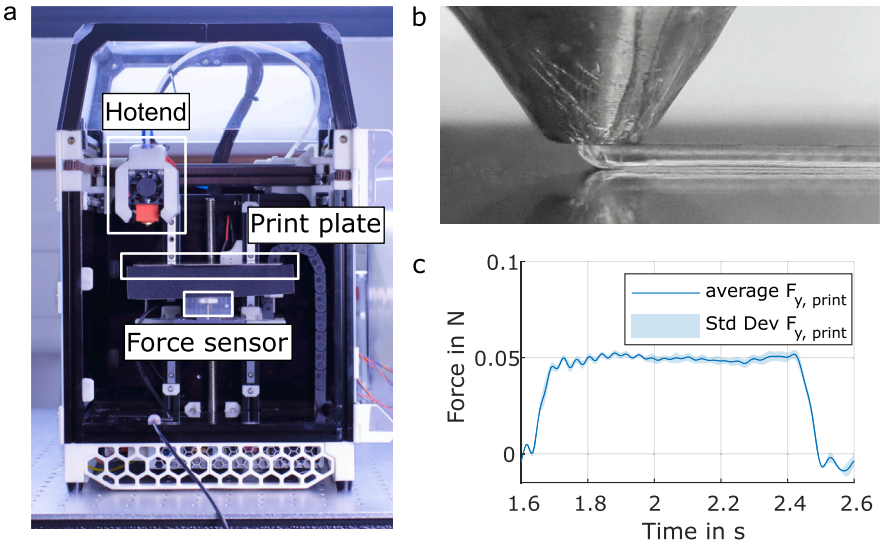

Fig. 4. Printing setup with a force sensor mounted below the print plate (a). A single printed line shows the extrusion flow (b). The force signal shows a plateau throughout one printed line (c).

2.1.3. Force measurement during 4DP

4DP is carried out with a Voron V0.1 3D printer. The printer has a CoreXY setup, a Bowden extruder, an E3D V6 hotend, and is equipped with a 0.4 mm nozzle. The print surface is a steel plate coated with Polyetherimide (PEI). The print plate is mounted on a 10N three-axis force sensor K3D40 10N (ME-Messsysteme, Germany). The sensor is connected to a measurement amplifier GSV-8DS SubD44HD (ME-Messsysteme, Germany), which is evaluated with the measurement software GSVmultichannel. The measurement frequency is 200 Hz. Simultaneously with the force measurement, the position is captured during the printing process with an ESP32 microcontroller connected to the motor drivers to collect the stepping signal. Every 5 ms, each microcontroller sends the print head's position, which results in a measurement frequency of 200 Hz. The whole setup is positioned on a vibration-controlled table to reduce outside vibrations. Fig. 4 displays the measurement setup.

The integrated force sensor has a nominal load capacity of 10 N and an accuracy class of 0.5, representing a compromise between robustness and sensitivity. To ensure statistical reliability, 15 lines are printed, and all data points within the force plateau are included in the boxplot evaluation, shown in Fig. 10. This results in a large number of samples, increasing the confidence in the measured trends.

The absolute force values depend on the calibration accuracy, which is influenced by linearity deviation (0.2% FS), zero-signal hysteresis (0.1% FS), and temperature effects (0.2% RD). Although noise was not quantitatively analyzed, the low-pass filtered signal exhibits minimal fluctuations during the printing of the lines, see Fig. 4(c). Overall, the integrated sensor provides stable and reliable force measurements.

Geometry & printing. The g-code is prepared with PrusaSlicer. The print is designed to print an initial line as a pre-extrusion line. Subsequently, five skirts are printed around the build plate to create a quasi-static extrusion. The print settings and the settings for the skirts are the same. Then, five 4D lines are printed. Each line has a height of 0.2 mm, a width of 0.45 mm, and a length of 80 mm. The volumetric flow is derived by the line's cross-section, therefore, it increases linearly with the printing speed, see Table 2. For the simulation parameters in Table 3, this results in a constant normalized nozzle speed. During printing, the printing force and nozzle position are measured. After the print, the build plate is removed from the printer for cooling, and an identical build plate is installed for the next print. Note that the experiments did not show pronounced die swell, see Fig. 4(b).

Achieving uniform extrusion conditions is a challenge, as even minor deviations can significantly affect the measured force. To minimize such effects, the nozzle–build-plate distance has to be calibrated through a surface scan of the build plate using the function in the *Klipper* firmware: *BED_MESH_CALIBRATE*, using the nozzle as a tactile probe and the integrated force sensor to detect surface contact. In addition, the filament feed was calibrated by extruding a 100 mm length of feedstock, which was accepted when the deviation was below 0.5%. This procedure improved the uniformity within individual prints and between consecutive print runs. Nevertheless, variations of up to ±10% in the gap height can still occur, leading to residual inconsistencies in extrusion or deposition.

Signal processing. The force signal contains noise and vibrations from the printer's fans and motors. Therefore, a lowpass filter with a pass-band frequency of 15 Hz is applied. Subsequently, the force signals

Table 2
Printing parameters for experiments. Note: The nozzle tip temperature T_{tip} is lower than the set nozzle temperature T_n due to heat distribution in the hotend. Furthermore, the build plate temperature varies slightly due to the heat introduced by the higher material temperature during deposition.

Category	Parameter	Value
Thermal parameters	Nozzle temperature T_n	200, 210, 220 °C
	Nozzle tip temperature T_{tip}	165, 171.5, 182 °C
	Build plate temperature T_b	turned off (≈ 26, 27.5, 29 °C)
	Ambient temperature T_a	≈ 25 °C
	Part cooling fan speed B	100%
Flow parameters	Nozzle diameter D	0.4 mm
	Printing speed V	20–100 mm s^{-1}
	Line width	0.45 mm
	Line height (Layer height)	0.2 mm
	Resulting volumetric flow	1.63 – 8.14 mm^3 s^{-1}

of the different prints are synchronized using the lags of the cross-correlation. Then, the position data is synchronized to the aligned force signals using the first movement in the z-direction. A spike in the force signal marks this first movement, due to the inertia of the build plate. Therefore, it gives good results for the synchronization of position and force data. After the signal processing, the dataset contains information about the measured force at different locations in each line. Finally, the mean force and standard deviation are calculated for each time step. This results in a singular signal for each line as shown in Fig. 4(b) and (c).

2.2. Numerical method

2.2.1. Governing equations

The thermofluid fields are governed by the Navier–Stokes equations and the heat equation, which can be rewritten using the Arbitrary Lagrangian-Eulerian (ALE) formulation as follows:

$$\begin{aligned} \nabla \cdot \mathbf{u} &= 0 \\ \rho \left(\left. \frac{\partial \mathbf{u}}{\partial t} \right|_{\chi} + (\mathbf{u} - \mathbf{u}_G) \cdot \nabla \mathbf{u} \right) - \nabla \cdot \boldsymbol{\sigma} &= \rho \mathbf{b} \\ \rho c_p \left(\left. \frac{\partial T}{\partial t} \right|_{\chi} + (\mathbf{u} - \mathbf{u}_G) \cdot \nabla T \right) - \nabla \cdot \kappa \nabla T - \phi &= 0 \end{aligned} \tag{2}$$

where $\mathbf{u}$, p, and T are the velocity, pressure, and temperature fields, respectively. The material properties are density ρ, viscosity η, thermal conductivity k, and specific heat capacity c_p. The stress tensor $\boldsymbol{\sigma} = -p\mathbf{I} + \boldsymbol{\tau}$ is divided into hydrostatic and viscous stress $\boldsymbol{\tau} = 2\eta\boldsymbol{\epsilon}$, which depends on the strain rate tensor $\boldsymbol{\epsilon} = \frac{1}{2}(\nabla\mathbf{u} + \nabla\mathbf{u}^T)$. Furthermore, $\mathbf{u}_G$ is the mesh velocity, $\mathbf{b}$ collects the body forces, and $\phi = 2\eta\nabla\mathbf{u} : \boldsymbol{\epsilon}$ is the viscous dissipation. Note that the viscosity depends on the temperature and shear rate $\dot{\gamma} = \sqrt{2\boldsymbol{\epsilon} : \boldsymbol{\epsilon}}$, and it is defined by the Cross-WLF viscosity model (1). χ is introduced to denote the ALE coordinate system. The governing equations are discretized in space by the finite element (FE) formulation, and in time by the implicit Euler method. The FE formulation is stabilized by the Galerkin/least-squares stabilization technique. The system of equations is linearized by the Newton–Raphson method and solved by the GMRES with ILUT preconditioner [70]. The solution strategy is performed in parallel and is based on distributed memory using the message-passing interface (MPI). The mesh deformation is performed by the well-known Elastic Mesh Update method (EMUM) [71]. This method treats the mesh as an elastic body occupying the domain $\Omega^{\#}$ with boundary $\Gamma^{\#}$, where the superscript # denotes the mesh. Thus, the displacement of the internal nodes $\mathbf{d}^{\#}$ is determined by solving the equations of linear elasticity $\nabla \cdot \boldsymbol{\sigma}^{\#} = \mathbf{0}$, where the stress tensor $\boldsymbol{\sigma}^{\#} = \lambda(\mathrm{tr}\boldsymbol{\epsilon}^{\#})\mathbf{I} + 2\mu\boldsymbol{\epsilon}^{\#}$ is related to the elastic strain tensor $\boldsymbol{\epsilon}^{\#} = \frac{1}{2}(\nabla\mathbf{d}^{\#} + (\nabla\mathbf{d}^{\#})^T)$ by the Lamé constants λ and μ. The mesh motion is enhanced by the surface-reconstruction virtual-region method (SRVR) [52], which is designed to handle the large displacements of the strand during deposition. SRVR utilizes the concept of a virtual region that divides the domain into an activated Ω_A and a deactivated Ω_D part. This approach allows to continuously enlarge the activated domain while elements are extruded. Note that the governing equations are solely solved in the activated domain Ω_A, i.e., the extruded strand. Additionally, a spline-based boundary representation is used to define curved boundaries. By constantly maintaining the boundary mesh nodes on an external spline, the mesh motion is restricted to slide over the spline's curved boundary. A detailed description of the numerical framework can be found in [50,51]. This framework is integrated into our in-house CFD finite element solver at RWTH Aachen University. All simulations were conducted in parallel on the CLAIX high-performance computing cluster at RWTH Aachen University.

2.2.2. Flow and thermal conditions

The computational domain is shown in Fig. 5(a). The shape of the three-dimensional mesh at the initial state is a cylinder with a rounded bottom surface, as shown in Fig. 5(b). The field Eqs. (2), i.e., flow and heat, are solved on the activated domain, as explained in Section 2.2.1. The activated domain Ω_A is enclosed by the free-surface Γ_f, the inlet Γ_i, and the part in contact with the nozzle tip Γ_s. Note that when the free-surface Γ_f is deposited on the build plate, a portion of Γ_f becomes Γ_c, taking the boundary conditions assigned to Γ_c. Due to the symmetry of the problem in the z-direction, only half of the filament is modeled.

The geometry of the nozzle tip is based on the nozzle design for the E3D V6 hotend. We modified the original geometry by smoothing out the sharp corner at the nozzle tip. In all simulations, a corner radius of 0.07 mm is used. It is important to mention that the curved shape of the nozzle tip is modeled with a spline-based boundary representation. Thus, the free surface can slide and detach from the boundary according to the fluid velocity. See [51] for more details.

The motion of the nozzle is modeled by including the nozzle speed V as a boundary condition on the build plate Γ_c. Thus, the nozzle stays fixed and the build plate moves along the x-direction at the nozzle speed V.

For the flow equation, a parabolic profile with an average extrusion velocity U is imposed at the inlet Γ_i. A wetting boundary condition is imposed on Γ_s. Such a condition is based on the Navier slip condition with a variable friction coefficient β. Thus, a slip condition is recovered in the vicinity of the contact line between Γ_s and Γ_f, and a nonslip condition elsewhere on Γ_s. A traction-free condition is imposed on the flow equation on the free surface Γ_f. On Γ_c, the boundary condition for the flow problem is a non-penetration condition with imposed velocity V in the x-direction. This is a no-slip condition in which the fluid moves at the substrate speed. Note that a contact detection algorithm is required to track the free-surface motion with respect to the bottom substrate. Given the complexity of implementing these boundary conditions, we direct the reader to our previous publications [50,51], which provide a detailed description of the implementation and validation.

The nozzle tip temperature T_{tip} is imposed on the inlet Γ_{in} and on the nozzle surface Γ_s. It was measured by a thermocouple at the nozzle tip and is 37 – 39 °C lower than the nozzle temperature set in the slicer. Therefore, the respective nozzle tip temperatures are specified in Table 3. On Γ_f and Γ_c, the strand is subject to cooling due to convection and conduction, respectively. The convection heat condition on Γ_{fs}, reads:

$$\mathbf{n} \cdot \nabla T = -h_c \left(T - T_a \right) \tag{3}$$

where h_c is the convection heat coefficient and T_a is the ambient temperature. In the case of conduction, thermal contact resistance between the strand and the build plate exists [61]. Thus, the thermal boundary conditions on Γ_c, reads:

$$\mathbf{n} \cdot \nabla T = -h_b \left(T - T_b \right) \tag{4}$$

where h_b is thermal contact conductance and T_b is the build plate temperature. The values of h_c and h_b will be determined in Section 3.1.1.

Table 3
Thermal, Process, and Material parameters for the simulation.

Category	Parameter	Value
Thermal parameters	Nozzle tip temperature T_{tip}	165, 171.5, 182 °C
	Build plate temperature T_b	26, 27.5, 29 °C
	Thermal conductance h_b	925 $\mathrm{W\,m^{-2}\,K^{-1}}$
	Ambient temperature T_a	25 °C
	Convective coefficient h_c	180 $\mathrm{W\,m^{-2}\,K^{-1}}$
Process parameters	Nozzle diameter D	0.4 mm
	Nozzle speed V	20 – 100 $\mathrm{mm\,s^{-1}}$
	Average extrusion velocity U	12.99 – 51.95 $\mathrm{mm\,s^{-1}}$
	Normalized nozzle speed V/U	1.54
	Gap height g	0.2 mm
	Normalized gap height g/D	0.5
Material parameters	Viscosity η	see Section 2.1.1
	Density ρ	1150 $\mathrm{kg\,m^{-3}}$
	Specific heat capacity c_p	2000 $\mathrm{J\,kg^{-1}\,K^{-1}}$
	Thermal conductivity k	0.195 $\mathrm{W\,m^{-1}\,K^{-1}}$

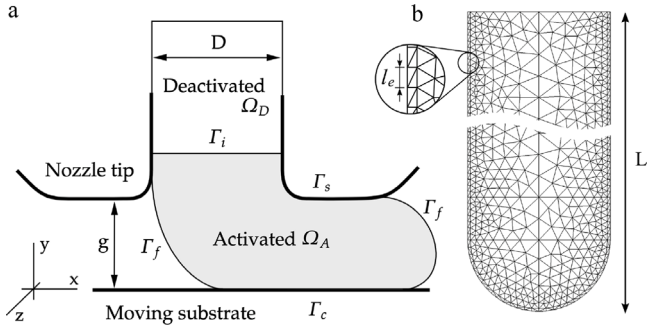

Fig. 5. Computational domain including dimensions, boundary conditions, and activated domain. External boundaries, such as the nozzle tip and the moving substrate, are represented by bold lines (a). Cross-sectional view of the tetrahedral mesh with a zoom in on the element at the wall that characterized the mesh (b).

The filament length is $L = 10D$, and the thermal, process, and material parameters can be found in Table 3. The influence of gravity and surface tension is neglected, as suggested in [45,59], respectively. The mesh is characterized by the element size l_e of the element at the wall, as shown in Fig. 5b. The other mesh dimensions are defined with respect to l_e, so when l_e changes, the whole mesh is scaled accordingly. The spatial refinement at the border has two primary purposes: better velocity definition at boundary nodes and small distortion of those elements due to the free surface motion [50].

One important quantity to compare with experiments is the printing force. This can be computed by considering the fluid shear force F over Γ_c in the tangential direction, which corresponds to the x-direction, as follows:

$$F = \int_{\Gamma_c} \mathbf{e}_x \cdot \boldsymbol{\sigma} \cdot \mathbf{n} \, \mathrm{d}\Gamma = \int_{\Gamma_c} \mathbf{e}_x \cdot \boldsymbol{\tau}_w \, \mathrm{d}\Gamma = \int_{\Gamma_c} \eta \frac{\partial u_x}{\partial y} \, \mathrm{d}\Gamma \tag{5}$$

where $\mathbf{e}_x$ is the basis vector in x-direction and $\mathbf{n}$ is normal vector to Γ_c. Furthermore, $\boldsymbol{\sigma} \cdot \mathbf{n}$ is the traction vector, from which only the tangential component contributes to the force F. The shear force is caused by the friction between the fluid and the surface, and it is represented by the wall shear stress $\boldsymbol{\tau}_w$. It is worth noting that such a quantity can be directly computed from the simulation, as we know the exact topology of the mesh that discretizes Γ_c.

3. Results and discussion

The following section first provides the numerical results. The experimental results are subsequently presented and then, compared and discussed considering the numerical results. Finally, the transformation upon activation is shown for the experimentally printed lines.

3.1. Numerical results

The main numerical results are obtained with the numerical framework introduced in Section 2.2.

3.1.1. Determination of heat transfer coefficients

We first start with the determination of the heat transfer coefficient. Such coefficients are crucial for accurately modeling the temperature profile of the filament during the printing process. Each coefficient is obtained by fitting the experimental data that describe the temperature decay of the filament as it is extruded, as illustrated in Section 2.1.2. The fitting process involved adjusting the convective coefficient h_c and conductance coefficient h_b in Eqs. (3) and (4) to fit the experimental temperature data within the standard deviation.

Throughout the fitting procedure, we observed that the heat transfer coefficients were dependent on the mesh size used in the simulation. To investigate this dependency, we perform a mesh convergence analysis using three different mesh sizes: coarse, medium, and fine. Each mesh information is detailed in Table 4.

Fig. 6 illustrates an example of the fitting process using the medium mesh. The IR measurement was repeated 5 times for statistical assurance. The black datapoints represent the average, and the whiskers are the standard deviation at the particular distance from the nozzle. The colored lines show the simulated temperature profiles and how they change at different heat transfer coefficients. In particular, the convective coefficient has a strong influence on the very beginning of the temperature profile, while the conductance coefficient has an impact on the subsequent progression. The same pattern was observed on the other mesh sizes, but they are not shown here. When analyzing the fitted convective coefficient h_c at different mesh sizes, we noticed low variability with a converged value of $h_c = 180\ \mathrm{W\,m^{-2}\,K^{-1}}$. On the contrary, the thermal conductance h_b shows significant variability, and the fitted values are presented in Table 4. Together with the studied meshes, the Richardson extrapolation (RE) is also presented. The Richardson extrapolation is commonly used in CFD simulations to perform mesh convergence analysis as it provides a higher-order estimated value at zero mesh size [72]. In particular, $h_{bRE} = 925\ \mathrm{W\,m^{-2}\,K^{-1}}$ is obtained, and this value will be used in further simulations.

In the literature, a wide range of heat transfer coefficients has been reported. The convection heat coefficient h_c typically ranges from 5 to 500 $\mathrm{W\,m^{-2}\,K^{-1}}$, while the thermal conductance h_b ranges from 88 to 4500 $\mathrm{W\,m^{-2}\,K^{-1}}$ [49,61,62,73–76]. This wide range of the coefficient can be attributed to environmental factors, the wettability of the polymer melt, adjacent boundaries, surface roughness, and local melt pressures [61]. It is important to note that radiation is neglected in this work since there is evidence that the radiation loss is negligible when the convective coefficient is larger than 60 $\mathrm{W\,m^{-2}\,K^{-1}}$ [73].

3.1.2. Mesh convergence analysis of the printing force

Once the heat transfer coefficients are obtained, we proceed to perform a mesh convergence analysis of the printing force F. Table 4 shows the results of the printing force when using $h_c = 180\ \mathrm{W\,m^{-2}\,K^{-1}}$ and $h_b = 925\ \mathrm{W\,m^{-2}\,K^{-1}}$. The Richardson extrapolation for the force is also presented. The results show that the force increases monotonically with finer mesh sizes. The absolute and relative errors are computed against the extrapolated force F_{RE}. The relative error decreases from 10.91% to 5.27% as the mesh size transitions from medium to fine. However, for this reduction, the computational effort notably increases. As a reference, a medium mesh simulation takes around 6 h while a fine mesh simulation takes 24 h on average. Therefore, for efficiency reasons, we decided to use the medium mesh for further simulations.

The relative error for the thermal conductance h_b and the printing force F is presented in Fig. 7. The relative error for the thermal conductance is higher than for the force. Nevertheless, both exhibit second-order convergence with respect to the element size. This matches the accuracy of the discretization of the governing equations.

Table 4
Mesh information of the meshes used in the simulations. Results of the mesh convergence analysis of the conductance coefficient and printing force.

Category	Parameter	Coarse	Medium	Fine	RE
Mesh information	Number of nodes	20,376	74,133	178,658	–
	Number of elements	92,131	350,081	879,291	–
	Mesh element size l_e in mm	0.0167	0.0114	0.0078	–
Conductance coefficient h_b	Fitted values in $\mathrm{W\,m^{-2}\,K^{-1}}$	1500	1200	1050	925
	Absolute error $\lvert h_b - h_{bRE}\rvert$	574.22	274.22	124.22	–
	Relative error $\lvert h_b - h_{bRE}\rvert / h_{bRE}$	62.03%	29.62%	13.42%	–
Printing Force F	Values in mN	31.14	36.68	39.00	41.28
	Absolute error $\lvert F - F_{RE}\rvert$	10.03	4.49	2.17	–
	Relative error $\lvert F - F_{RE}\rvert / F_{RE}$	24.36%	10.91%	5.27%	–

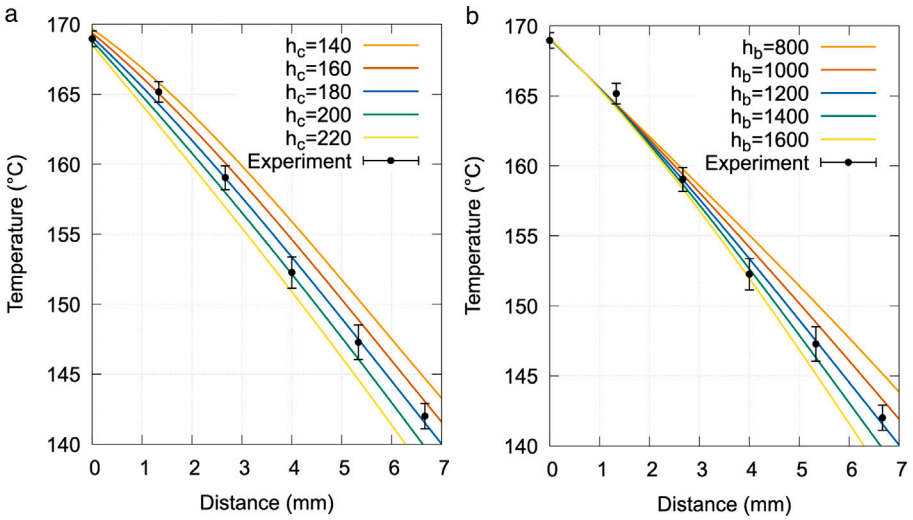

Fig. 6. Temperature decay of the filament as it is extruded. Numerical results at different heat transfer coefficients using the medium mesh are plotted with lines, and experimental results from the IR measurement are plotted with points and whiskers.

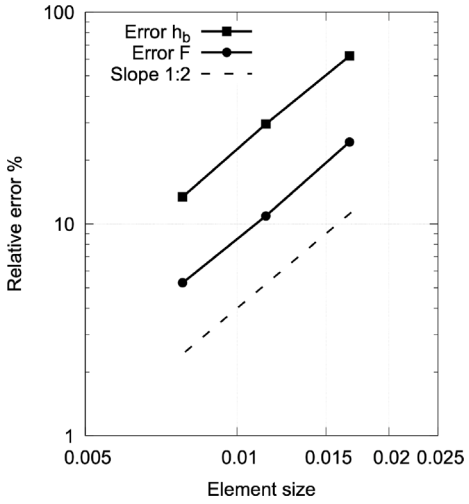

Fig. 7. Relative error of the conductance coefficient and printing force at different element sizes.

3.1.3. Sensitivity analysis

A sensitivity analysis of the main printing parameters helps to evaluate and classify the obtained results. For this analysis, all simulations are performed under a standard set of printing conditions, modifying only one parameter at a time. Table 5 shows the list of parameters studied, their value, the resulting force, and the corresponding variation. Among the parameters studied, the sensitivity analysis shows that the volumetric flow, the gap height, and the nozzle temperature have an important impact on the resulting force. Meanwhile, the effects of both heat transfer coefficients h_c and h_b and the nozzle speed on the force are minor. The volumetric flow variation is computed with respect to the tolerance of the filament's diameter given by the manufacturer of 1.75 ± 0.05 mm. As a result, the force exhibits a variation of up to 5.2%. The gap height is evaluated with variations of 5%, resulting in a force variation up to 14.28% when g increases by 10%. The nozzle tip temperature is the parameter that shows the most significant effect on the resulting force, with force variation up to 22.51% when the temperature increases by 7.87%. This parameter will be further studied in the next section. Additionally, both heat transfer coefficients show a negligible influence on the force, as the convective coefficient shows the least effect. The nozzle speed also exhibits a minor influence with a force variation of up to 3.6% when the nozzle speed increases by 10%.

A comparison between isothermal and non-isothermal modeling is also carried out. It is important to recall that, without the thermal model, the isothermal case omits two physical effects: temperature-dependent viscosity and viscous dissipation. For the isothermal case, the viscosity at 220 °C is set as zero viscosity for the Cross model. The printing force and the computational cost for two nozzle speeds are shown in Table 6. The results show that the isothermal simplification introduces a small but non-negligible error in force prediction without providing a significant performance gain. In particular, the isothermal force differs from the non-isothermal one by up to 6.56% with a 4.88% decrease in total computing time. Although the polymer melt spends a short time under the nozzle, it is sufficient to modify the thermofluid behavior and, therefore, the printing force.

Table 5
Sensitivity analysis of different printing parameters. Each parameter value, the resulting force, and the corresponding variations are presented.

Parameter	Value	Variation	Force in mN	Variation
Convective coefficient h_c in $\mathrm{W\,m^{-2}\,K^{-1}}$	140	−22.2%	37.59	0.39%
	180	0%	37.44	0%
	220	22.2%	37.45	0.03%
Thermal conductance h_b in $\mathrm{W\,m^{-2}\,K^{-1}}$	1000	−16.67%	37.01	−1.15%
	1200	0%	37.44	0%
	1400	16.67%	37.84	1.06%
Volumetric flow in $\mathrm{mm^3/s}$	6.14	−5.63%	35.50	−5.20%
	6.51	0%	37.45	0%
	6.89	5.80%	38.28	2.23%
Gap height g in mm	0.180	−10%	41.63	11.18%
	0.190	−5%	39.35	5.09%
	0.200	0%	37.45	0%
	0.210	5%	34.14	−8.84%
	0.220	10%	32.10	−14.28%
Nozzle speed V in mm/s	72	−10%	37.44	−0.03%
	76	−5%	37.23	−0.59%
	80	0%	37.45	0%
	84	5%	36.85	−1.60%
	88	10%	36.10	−3.60%
Nozzle tip temperature in °C	165	−3.79%	43.28	17.35%
	171.5	0%	36.88	0%
	182	7.87%	28.58	−22.51%

Table 6
Sensitivity analysis of isothermal and non-isothermal cases. The resulting force, computing time, and the corresponding variations are presented.

Case	V in mm/s	Force in mN	Variation	Computing time in s	Variation
Isothermal	20	12.99	−6.56%	1.89×10^4	−4.88%
Non-isothermal		13.90	0%	1.99×10^4	0%
Isothermal	100	29.98	−4.76%	2.67×10^4	−3.36%
Non-isothermal		31.48	0%	2.77×10^4	0%

3.1.4. Shear rate analysis

The distribution of shear rate during the printing process and the wall shear stress on the build plate are illustrated in Fig. 8, which reveals highly heterogeneous distributions. As the fluid approaches the nozzle exit, the shear rate increases, reaching its peak just before the fluid detaches from the nozzle. This behavior is particularly important for shear-thinning materials, where the shear rate plays a critical role in determining the decrease in viscosity with increasing shear rate.

In Fig. 8(b), we observe that the shear rate experiences a significant spike near the nozzle inside wall, while in the rest of the domain, the shear rate remains relatively low. Notably, there is also an increase in shear rate upon contact with the build plate; however, this increase is of lower magnitude compared to the maximum near the nozzle. This effect is further detailed in Fig. 8(c) and (d).

Fig. 8(c) and (d) present the shear rate and wall shear stress along the x-direction as viewed from the bottom. The wall shear stress serves as a key quantity in calculating the resulting force, as outlined in Eq. (5). A comparison of both distributions shows that elevated shear and wall shear stress values are concentrated when the fluid makes contact with the bottom wall, with lower values observed further away from it. A resurgence of wall shear stress is noted, albeit to a lesser extent.

This finding is significant as it establishes a connection between the shear rate, the wall shear stress, and the resulting force. The concentration of wall shear stress at the front of the deposition indicates that the main component of the fluid shear force is located specifically there. This also explains why the nozzle temperature has a significant effect on the force, rather than the heat transfer coefficients. While the heat transfer coefficient influences the temperature decay later on, the temperature at the front of the deposition is primarily governed by the nozzle temperature. Thus, the nozzle temperature, together with the shear rate, dictates the viscosity of the material and consequently influences the fluid shear force.

3.2. Experimental results

The main results are obtained with the experiments that are described in Section 2.1.

3.2.1. Force signal during printing

The force signal of the sample series printed with $T_n = 200$ °C and $V = 100$ mm s−1 (Series T200-V100 in the following) shows the individual printed lines, see Fig. 9. After each line, the abrupt movement of the print head leads to an oscillation, which is reflected in the force signal. When the next line is printed, the oscillation decays and can be neglected. The data shows that positive and negative printing directions have similar force plateaus. The absolute values of the plateaus are used for the statistical evaluation in Fig. 10. In addition, the standard deviation over the three repeated prints is very low for all lines and all specimen series. In this specimen series, the fifth line has the largest standard deviation of 0.0046N. In conclusion, the average force is reliable and repeatable and will be used for the comparison of the specimen series.

3.2.2. Printing force dependencies

The boxplot of all specimen series shows that the median plateau force of a printed PLA line is between 0.0084 N (Series T220-V20) and 0.0462 N (Series T200-V100), see Fig. 10(a). The notch in the boxplot represents the 95% confidence interval for the median. Therefore, it is evident that the median forces differ significantly from those of other series. The three series with $V = 20$ mm s^{-1} have the lowest median force for the respective nozzle Temperature. The force increases with increasing speed. Furthermore, an increasing nozzle temperature T_n decreases the printing force.

The average force values in Fig. 10(b) support the findings from the boxplot and displays the effect of printing speed for the respective

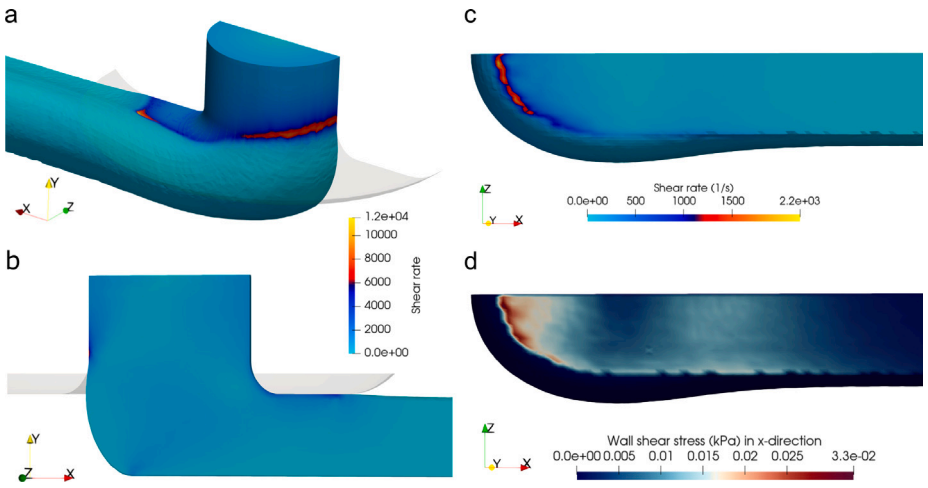

Fig. 8. Shear rate distribution during deposition (a-c) and wall shear stress in x-direction at the bottom surface during deposition (d).

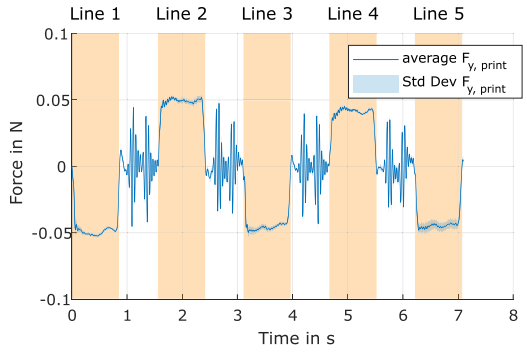

Fig. 9. The force signal of the displayed specimen series (T_n = 200 °C and V = 100 mm s^{-1}) has 5 lines. Each line can be identified by the force plateau. The three prints show a small standard deviation in the force-time data.

temperatures in relation. For the speeds 40, 60, and 80 mm s^{-1}, the curve is linear and parallel for the three temperatures. Below this range, the gradient is greater at 200 °C and less at 220 °C than within the range. Above this range, the gradient is also greater at 200 °C and less at 220 °C. Only for 210 °C is the increase linear throughout.

In the printing speed range from 40 to 80 mm s^{-1}, the curve progression is parallel. In this region, reducing the temperature from 220 to 210 °C has a smaller effect on the force than reducing the temperature from 210 to 200 °C. This observation follows the expected behavior of the WLF and the Arrhenius equation. However, outside this printing speed range, the trend does not follow the expected behavior.

3.3. Discussion of experimental and numerical results

The numerical results reproduce the measured forces well. Notably, the simulated force range (13.9 – 46.4 mN) closely matches the experimental range (8.9 – 46.1 mN), indicating good agreement between simulation and experiment within the investigated conditions.

However, differences arise in the qualitative trends with printing speed. In the experiments, the force increases approximately linearly at medium speeds, while at the low nozzle temperature (200 °C) the gradient is steeper for both low (20–40 mm s^{-1}) and high speeds (80–100 mm s^{-1}). At the higher nozzle temperature (220 °C), this gradient becomes flatter in both speed ranges. In contrast, the simulation also predicts an increasing force with speed, but the slope decreases consistently for all temperatures. Increasing the printing speed in the simulation effectively raises the average shear rate. Therefore, one factor of this degressive trend in the force originates from the Cross–WLF model, which reduces the viscosity as the shear rate increases, see Fig. 2(c).

A second difference concerns the temperature sensitivity. For a nozzle speed of V = 60 mm s^{-1}, the experimental force ratio between 220 and 210 °C is $R_{F,\mathrm{exp}} \approx 22.8/19.1 \approx 1.19$, compared to the numerical ratio $R_{F,\mathrm{num}} \approx 33.0/25.0 \approx 1.32$. Hence, the simulated force increase at higher temperatures is more pronounced than in the experiment. Conversely, between 210 and 200 °C, the experimental ratio ($R_{F,\mathrm{exp}} \approx 30.0/22.8 \approx 1.32$) is higher than the numerical ratio ($R_{F,\mathrm{num}} \approx 38.9/33.0 \approx 1.18$), indicating stronger temperature sensitivity in the experiment at low temperatures.

These discrepancies likely arise from physical effects not captured by the Cross–WLF model, such as partial melting or thermal gradients within the nozzle. At high speeds or low nozzle temperatures, the polymer may experience insufficient melting time, effectively increasing the local viscosity.

Overall, both experimental and numerical results follow the expected trends: (i) increasing nozzle temperature reduces the printing force, and (ii) increasing printing speed increases it. However, a quantitative comparison reveals increasing deviations at lower printing speeds (see Table 7). Relative errors of 92.24% (Series T200–V20), 98.49% (Series T210–V20), and 55.83% (Series T220–V20) are observed, whereas at higher printing speeds the discrepancy decreases substantially to 0.74% (Series T200–V100), 16.35% (Series T210–V100), and 16.12% (Series T220–V100). Across all parameter sets, the numerical model systematically overestimates the experimentally measured printing force.

This overestimation can be attributed to simplifying assumptions inherent to the numerical framework and experimental uncertainties. First, the model enforces a perfect adhesion condition between the deposited filament and the build plate, which can increase local shear rates, consequently, the simulated force. Second, the nozzle tip temperature applied in the simulation may be lower than the actual melt temperature, due to heating in the larger-diameter filament section. An underestimated material temperature would result in an overpredicted viscosity and, thus, a higher simulated printing force. Third, discrepancies may arise from experimental factors. Machine compliance can introduce small misalignments between the actual printing direction and the force measurement axis, leading to a lower measured printing force.

While these results demonstrate that printing force trends correlate consistently, the simulation does not provide a quantitative prediction. Furthermore, the simulation does not resolve shape programming, which would require a viscoelastic model, allowing stress storage and

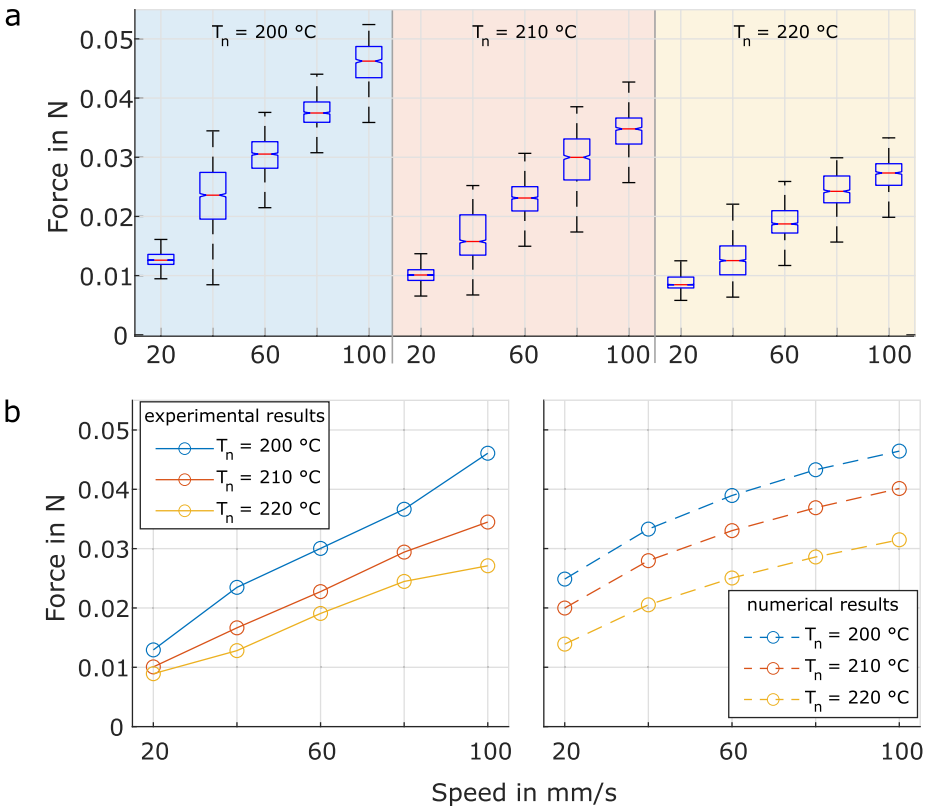

Fig. 10. The experimental results show that the specimen series differ significantly (a). The notch of the boxplot covers the 95%-confidence-interval for the median. Furthermore, the average values provide insight into the effect of nozzle speed and temperature (b).

Table 7
Force at different speeds and temperatures. Important process parameters such as the normalized nozzle speed and the normalized gap height are kept constant in the experiment and simulation.

	Nozzle temperature					
	200 °C		210 °C		220 °C	
Speed V	Forces in mN					
	exp.	sim.	exp.	sim.	exp.	sim.
20 mm/s	12.932	24.860	10.066	19.980	8.920	13.900
40 mm/s	23.473	33.280	16.652	27.960	12.809	20.520
60 mm/s	30.037	38.940	22.755	33.020	19.076	25.040
80 mm/s	36.639	43.280	29.417	36.880	24.472	28.580
100 mm/s	46.081	46.420	34.482	40.120	27.111	31.480

relaxation. Accordingly, the printing force is only a process-level indicator of flow resistance, and not a predictor of flow-induced pre-strain (see Table 7).

3.4. Transformation of 4D printed lines

Thermal activation is the inherent post-processing step in FDM-based 4DP. It triggers the programmed transformation of the smart structure, which can manifest as bending, contraction, or torsion. The activation conditions ultimately determine the speed and magnitude of this transformation, as they influence heating rate, viscoelastic relaxation, and environmental interactions. In this study, all specimens were thermally activated at 80 °C for 10 min in a convection oven, see Table 8. Each single-line specimen was clamped at the top and freely suspended to ensure a consistent gravitational load. The convection fan was switched off to avoid airflow-induced disturbances during transformation. All activation parameters were kept constant across specimen series, ensuring that differences in the transformation arise solely from variations in the printing parameters.

Table 8
Activation parameters for shape transformation.

Activation medium	Air (convection oven)
Activation temperature	80 °C
Activation time	10 min

The thermal activation in the convection oven causes the printed lines to coil, see Fig. 11(a). For all specimens, the outer side of the coil is the top surface, and the inner side of the coil is the bottom surface. Therefore, the bottom surface of the line shrinks more than the top. The helix occurs due to the gravitational force of the coiled material, which causes a rotation along the line's axis. Gravity also causes the distance between turns to decrease towards the right end of the helix, see Fig. 11(a). Fig. 11(b) shows that only small curvatures occur for $v_p = 20$ mm/s and no helix is formed. With increasing printing speed v_p, curvature increases, and a helix is formed due to gravity. The curvature is also positively affected by a lower nozzle temperature. However, the effect of nozzle temperature T_n appears to be less significant than that of printing speed in the investigated range, see Fig. 11.

The shape transformation of the lines confirms that the printing process affects the spatial arrangement of polymer chains, i.e., the polymer conformation. First, the polymer chains are oriented during the printing process, due to the flow of the melt inside the nozzle and in the corner flow [41]. Second, the flow of the melt also stretches the individual chains. In a physical sense, the entropy of the chains is reduced. Third, this conformation is rapidly frozen and therefore stored in the printed lines [44]. The deviation from the equilibrium conformation causes the shape change during activation and is driven by entropy.

The coil shape reveals that the bottom side has more deviation from equilibrium conformation than the top side and has more shape-changeability stored. This correlates with the experimental and numerical temperature history of the singular line as the bottom side

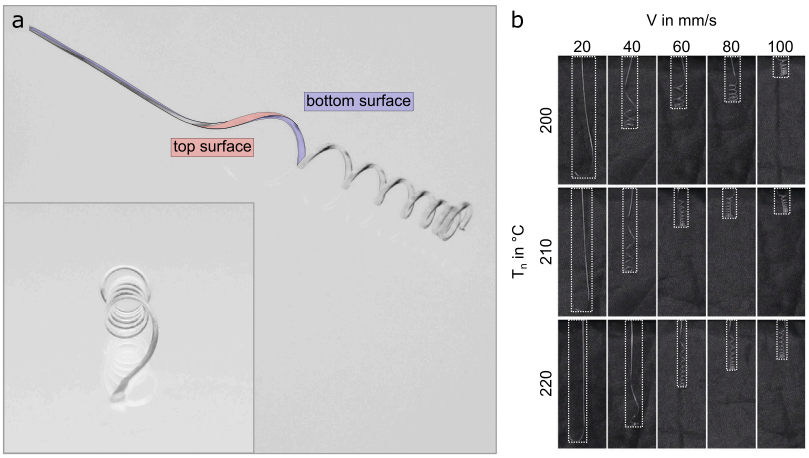

Fig. 11. The activation causes the 4D printed lines to coil. The inner side of the coil is the bottom surface. The outer side of the coil is the top surface (a). The printing speed V and the nozzle temperature T_n have a major effect on the amount of shrinkage (b).

cools faster than the top, shown by the large conductive transfer coefficient vs. the small convective coefficient. The faster cooling of the bottom decreases the amount of relaxation potential. Furthermore, McIlroy and Olmstedt argue with their viscoelastic model that the increased path length and larger deformation due to the redirection during deposition play an important role in the conformation difference between the bottom and top side of a printed line, leading to a residual stress difference [44]. However, the fluid simulation of this study only derives pressure and velocity fields based on a purely viscous material model and cannot predict residual stresses. Therefore, the simulated printing force is not a direct predictor of the non-equilibrium conformation, but macroscopically, numerical and experimental printing forces qualitatively correlate with the transformation magnitude.

4. Conclusion

This work advances the understanding of 4DP using FDM by combining experimental and numerical approaches. The study introduces the perspective of the shape-memory cycle to interpret 4DP, allowing a qualitative connection between process conditions, printing force, and subsequent shape recovery behavior. Because experimental methods provide only discrete force measurements and limited access to in-process states, a numerical framework was developed to gain deeper insight into flow and thermal fields. It must be noted that the numerical framework only provides printing force and not residual stresses since a purely shear-thinning Cross-WLF model is used. Within this framework, key parameters were identified, heat-transfer coefficients were determined, and a Cross–WLF viscosity model for PLA was calibrated.

The sensitivity analysis reveals that gap height, nozzle temperature, and volumetric flow are the most influential parameters governing the printing force. The results highlight the importance of precisely controlling these parameters to avoid experimental deviations. Adapting printer design can improve gap height and nozzle temperature accuracy, but cannot compensate for filament diameter variations. Therefore, filament manufacturers must ensure accurate diameters to improve 4DP. Although printing speed is less sensitive, it can be varied continuously in a wide range ($0 - 100$ mm s^{-1}), making it an effective design variable for tuning the behavior of 4D printed structures. The numerical shear-rate distributions showed maxima at the nozzle exit and deposition-front-build-plate interface, highlighting the regions where material strain and fluid shear stresses are most critical.

The sensitivity analysis also reveals that both heat transfer coefficients have a minor effect on the simulated printing force. Although the heat coefficients influence temperature decay along the printing line, the nozzle temperature has a greater impact on the printing force. This finding is significant for our study because obtaining the heat coefficients can be challenging, as it requires a precise procedure that involves IR temperature measurements and fitting the simulations to the measurements. This insight could be useful in future studies by reducing the effort required to determine the exact heat transfer coefficients, as approximate values would also be acceptable.

The comparison between isothermal and non-isothermal modeling reveals that neglecting thermal effects leads to a small but non-negligible error in force prediction, up to 6.56%, without providing a significant performance gain. These findings demonstrate that even during the brief period the polymer melt spends under the nozzle, thermal variations influence thermofluid behavior for the conditions considered in this study. As a result, the loss in force prediction accuracy with minimal computational time savings does not justify the isothermal assumption.

McIlroy and Olmsted analytically predicted, using a viscoelastic model, that the bottom side of a printed line experiences a higher level of stored pre-strain [41,44]. Lukhi et al. reported consistent findings based on a multiphysics simulation framework for predicting residual stress in viscoelastic materials and further supported their predictions through a limited experimental study [49]. The present work extends these prior studies by providing broader experimental evidence across a wider range of printing parameters, thereby supporting the existence of a layerwise pre-strain gradient within printed lines.

The present study is limited to predicting the printing force and is restricted to the single-line deposition case. First, the numerical model employs a shear-thinning viscosity formulation and therefore does not resolve viscoelastic effects, such as residual stress or stored pre-strain. As a result, the predicted printing forces represent the flow resistance during extrusion and deposition rather than the residual stress state of the material. Nevertheless, the numerical and experimental results show good quantitative agreement, providing a clear reference for trends in increasing or decreasing printing force. Moreover, experimental printing forces have been shown to correlate with the magnitude of shape transformation during activation, as previously demonstrated by Cerbe et al. [32]. Consequently, this work represents a step towards establishing quantitative experimental measures that can be used in the future to corroborate viscoelastic simulations predicting residual stress formation.

Second, both the experiments and simulations are restricted to single-line deposition, whereas multi-line single-layer and multi-line multi-layer cases introduce additional physical effects caused by the boundary conditions. In multi-line single-layer printing, intralayer heat transfer becomes significant and introduces additional lateral boundaries. In multi-line multi-layer printing, interlayer reheating leads to a cumulative thermal history, causing thermal loads and stress relaxation, while the presence of underlying layers introduces a bottom boundary

that affects both heat transfer and interlayer adhesion. These effects are not captured in the present single-line framework and should be addressed in future studies.

Future work will focus on extending the current Cross-WLF to a viscoelastic material model that accounts for temperature- and strain-dependent material history, enabling prediction of frozen-in residual stresses. Achieving this capability can provide guidelines for controlling or tailoring residual stresses in printed parts. Furthermore, ongoing research aims to study multi-layer structures, where repeated heating during overprinting causes relaxation and influences the stress state of the final smart structure. Combining experimental–numerical strategies will help identify the dominant factors governing residual stress, guiding sensor integration and design improvements for industry-ready 4D printers.

CRediT authorship contribution statement

Ferdinand Cerbe: Writing – original draft, Validation, Investigation, Formal analysis, Data curation, Conceptualization. **Felipe A. González:** Writing – original draft, Software, Investigation, Formal analysis, Conceptualization. **Michael Sinapius:** Writing – review & editing, Supervision, Resources, Funding acquisition. **Marek Behr:** Writing – review & editing, Resources, Funding acquisition. **Stefanie Elgeti:** Writing – review & editing, Supervision.

Data statement

The data that support the findings of this study are available from the corresponding author upon reasonable request.

Declaration of Generative AI and AI-assisted technologies in the writing process

During the preparation of this work, the authors used AI-assisted technologies in order to review the language and clarity of this article. After using this tool, the authors reviewed and edited the content as needed and take full responsibility for the content of the published article.

Funding information

Funded by the Deutsche Forschungsgemeinschaft (DFG, German Research Foundation) – Project numbers 447858794; 566317635. The authors gratefully acknowledge the German Federal Ministry of Research, Technology, and Space (BMFTR) and the state of North Rhine-Westphalia for supporting this work as part of the NHR funding.

Declaration of competing interest

The authors declare that they have no known competing financial interests or personal relationships that could have appeared to influence the work reported in this paper.

Data availability

Data will be made available on request.

References

[1] Skylar Tibbits, 4D printing: Multi–material shape change, Archit. Des. 84 (1) (2014) 116–121, http://dx.doi.org/10.1002/ad.1710.
[2] Muhammad Yasir Khalid, Zia Ullah Arif, Reza Noroozi, Ali Zolfagharian, Mahdi Bodaghi, 4D printing of shape memory polymer composites: A review on fabrication techniques, applications, and future perspectives, J. Manuf. Process. 81 (2022) 759–797, http://dx.doi.org/10.1016/j.jmapro.2022.07.035.
[3] Somayeh Vatanparast, Alberto Boschetto, Luana Bottini, Paolo Gaudenzi, New trends in 4D printing: a critical review, Appl. Sci. 13 (13) (2023) 7744, http://dx.doi.org/10.3390/app13137744.
[4] Qi Ge, H. Jerry Qi, Martin L. Dunn, Active materials by four-dimension printing, Appl. Phys. Lett. 103 (13) (2013) 131901, http://dx.doi.org/10.1063/1.4819837.
[5] Mahdi Bodaghi, Alireza D. Damanpack, Wei-Hsin Liao, Self-expanding/shrinking structures by 4D printing, Smart Mater. Struct. 25 (10) (2016) 105034, http://dx.doi.org/10.1088/0964-1726/25/10/105034.
[6] Jennie Ryu, Matteo D'Amato, Xiaodong Cui, Kevin N. Long, H. Jerry Qi, Martin L. Dunn, Photo-origami—Bending and folding polymers with light, Appl. Phys. Lett. 100 (16) (2012) 161908, http://dx.doi.org/10.1063/1.3700719.
[7] Jesús Del Barrio, Carlos Sánchez-Somolinos, Light to shape the future: From photolithography to 4D printing, Adv. Opt. Mater. 7 (16) (2019) http://dx.doi.org/10.1002/adom.201900598.
[8] Han Liu, Feifan Wang, Wenyang Wu, Xufeng Dong, Lin Sang, 4D printing of mechanically robust PLA/TPU/Fe3O4 magneto-responsive shape memory polymers for smart structures, Compos. Part B: Eng. 248 (2023) 110382, http://dx.doi.org/10.1016/j.compositesb.2022.110382.
[9] Jun Wang, Xiang Lin, Runguo Wang, Yonglai Lu, Liqun Zhang, Self–healing, photothermal–responsive, and shape memory polyurethanes for enhanced mechanical properties of 3D/4D printed objects, Adv. Funct. Mater. 33 (15) (2023) http://dx.doi.org/10.1002/adfm.202211579.
[10] Dan Raviv, Wei Zhao, Carrie McKnelly, Athina Papadopoulou, Achuta Kadambi, Boxin Shi, Shai Hirsch, Daniel Dikovsky, Michael Zyracki, Carlos Olguin, Ramesh Raskar, Skylar Tibbits, Active printed materials for complex self-evolving deformations, Sci. Rep. 4 (2014) 7422, http://dx.doi.org/10.1038/srep07422.
[11] Rytis Mitkus, Ultraviolet Light Curable Piezoelectric Multi-phase Composites, Springer Nature Switzerland, Cham, 2024, http://dx.doi.org/10.1007/978-3-031-56946-3.
[12] Rytis Mitkus, Ferdinand Cerbe, Michael Sinapius, 4D printing electro-induced shape memory polymers, in: Mahdi Bodaghi, Ali Zolfagharian (Eds.), Smart Materials in Additive Manufacturing Volume 2, in: Additive Manufacturing Materials and Technologies Ser, ELSEVIER, San Diego, 2022, pp. 19–51.
[13] Hesam Soleimanzadeh, Bernard Rolfe, Mahdi Bodaghi, Marzieh Jamalabadi, Xiang Zhang, Ali Zolfagharian, Sustainable robots 4D printing, Adv. Sustain. Syst. 7 (12) (2023) 2300289, http://dx.doi.org/10.1002/adsu.202300289.
[14] Ijaz Akbar, Mourad El Hadrouz, Mohamed El Mansori, Dimitri Lagoudas, Toward enabling manufacturing paradigm of 4D printing of shape memory materials: Open literature review, Eur. Polym. J. 168 (2022) 111106, http://dx.doi.org/10.1016/j.eurpolymj.2022.111106.
[15] Xueli Zhou, Luquan Ren, Zhengyi Song, Guiwei Li, Jifeng Zhang, Bingqian Li, Qian Wu, Wangxuan Li, Lei Ren, Qingping Liu, Advances in 3D/4D printing of mechanical metamaterials: From manufacturing to applications, Compos. Part B: Eng. 254 (2023) 110585, http://dx.doi.org/10.1016/j.compositesb.2023.110585.
[16] Chengjun Zeng, Liwu Liu, Yunqiang Hu, Wei Zhao, Xiaozhou Xin, Yanju Liu, Jinsong Leng, Stair–stepping mechanical metamaterials with programmable load plateaus, Adv. Funct. Mater. 34 (49) (2024) http://dx.doi.org/10.1002/adfm.202408887.
[17] Ramisha Sajjad, Sohaib Tahir Chauhdary, Muhammad Tuoqeer Anwar, Ali Zahid, Azhar Abbas Khosa, Muhammad Imran, Muhammad Haider Sajjad, A review of 4D printing–technologies, shape shifting, smart polymer based materials, and biomedical applications, Adv. Ind. Eng. Polym. Res. 7 (1) (2024) 20–36.
[18] Ferdinand Cerbe, Michael Sinapius, Markus Böl, Methodology for FDM 4D printing with thermo-responsive SMPs, Mater. Today: Proc. (2022) http://dx.doi.org/10.1016/j.matpr.2022.11.440.
[19] Hesam Soleimanzadeh, Mahdi Bodaghi, Marzieh Jamalabadi, Bernard Rolfe, Ali Zolfagharian, Rotary 4D printing of programmable metamaterials on sustainable 4d mandrel, Adv. Mater. Technol. 11 (1) (2026) http://dx.doi.org/10.1002/admt.202501581.
[20] Teunis van Manen, Shahram Janbaz, Amir A. Zadpoor, Programming 2D/3D shape-shifting with hobbyist 3D printers, Mater. Horizons 4 (6) (2017) 1064–1069, http://dx.doi.org/10.1039/c7mh00269f.
[21] Byoungkwon An, Ye Tao, Jianzhe Gu, Tingyu Cheng, Xiang 'Anthony' Chen, Xiaoxiao Zhang, Wei Zhao, Youngwook Do, Shigeo Takahashi, Hsiang-Yun Wu, Teng Zhang, Lining Yao, Thermorph: Democratizing 4D printing of self-folding materials and interfaces, in: Regan Mandryk, Mark Hancock, Mark Perry, Anna Cox (Eds.), Proceedings of the 2018 CHI Conference on Human Factors in Computing Systems, ACM, New York, NY, USA, 2018, pp. 1–12, http://dx.doi.org/10.1145/3173574.3173834.

[22] Akihiro Nojiri, Eiji Iwase, Michinao Hashimoto, Self-assembly of shape memory polymer printed by fused deposition modeling, in: S. Takeuchi, J.-B. Yoon (Eds.), 2019 IEEE 32nd International Conference on Micro Electro Mechanical Systems, MEMS, IEEE, 2019, pp. 380–383, http://dx.doi.org/10.1109/MEMSYS.2019.8870849.

[23] Dilip Chalissery, Dennis Schönfeld, Mario Walter, Inga Shklyar, Heiko Andrae, Christoph Schwörer, Tobias Amann, Linda Weisheit, Thorsten Pretsch, Highly shrinkable objects as obtained from 4D printing, Macromol. Mater. Eng. 307 (1) (2022) 2100619, http://dx.doi.org/10.1002/mame.202100619.

[24] Yousif Saad Alshebly, Marwan Nafea, Effects of printing parameters on 4D-printed PLA actuators, Smart Mater. Struct. 32 (6) (2023) 064008, http://dx.doi.org/10.1088/1361-665X/acd504.

[25] Quan Zhang, Dong Yan, Kai Zhang, Gengkai Hu, Pattern transformation of heat-shrinkable polymer by three-dimensional (3D) printing technique, Sci. Rep. 5 (2015) 8936, http://dx.doi.org/10.1038/srep08936.

[26] Abishera Ravichandra Rajkumar, Kumar Shanmugam, Additive manufacturing-enabled shape transformations via FFF 4D printing, J. Mater. Res. 33 (24) (2018) 4362–4376, http://dx.doi.org/10.1557/jmr.2018.397.

[27] Mahdi Bodaghi, Wei-Hsin Liao, 4D printed tunable mechanical metamaterials with shape memory operations, Smart Mater. Struct. 28 (4) (2019) 045019, http://dx.doi.org/10.1088/1361-665X/ab0b6b.

[28] Lukas Kačergis, Rytis Mitkus, Michael Sinapius, Influence of fused deposition modeling process parameters on the transformation of 4D printed morphing structures, Smart Mater. Struct. 28 (10) (2019) 105042, http://dx.doi.org/10.1088/1361-665X/ab3d18.

[29] Guanyun Wang, Tingyu Cheng, Youngwook Do, Humphrey Yang, Ye Tao, Jianzhe Gu, Byoungkwon An, Lining Yao, Printed paper actuator, in: Regan Mandryk, Mark Hancock, Mark Perry, Anna Cox (Eds.), Proceedings of the 2018 CHI Conference on Human Factors in Computing Systems, ACM, New York, NY, USA, 2018, pp. 1–12, http://dx.doi.org/10.1145/3173574.3174143.

[30] Jianzhe Gu, Vidya Narayanan, Guanyun Wang, Danli Luo, Harshika Jain, Kexin Lu, Fang Qin, Sijia Wang, James McCann, Lining Yao, Inverse design tool for asymmetrical self-rising surfaces with color texture, in: Emily Whiting, John Hart, Cynthia Sung, Nadya Peek, Masoud Akbarzadeh, Dan Aukes, Adriana Schulz, Hayden Taylor, Jeeeun Kim (Eds.), Symposium on Computational Fabrication, ACM, New York, NY, USA, 2020, pp. 1–12, http://dx.doi.org/10.1145/3424630.3425420.

[31] Yanan Wang, Xiang Li, 4D-printed bi-material composite laminate for manufacturing reversible shape-change structures, Compos. Part B: Eng. 219 (2021) 108918, http://dx.doi.org/10.1016/j.compositesb.2021.108918.

[32] Ferdinand Cerbe, Dominik Mahlstedt, Michael Sinapius, Christian Hühne, Markus Böl, Relationship between programming stress and residual strain in FDM 4D printing, Prog. Addit. Manuf. (2024) http://dx.doi.org/10.1007/s40964-023-00477-w.

[33] Mahdi Bodaghi, Alireza D. Damanpack, Wei-Hsin Liao, Adaptive metamaterials by functionally graded 4D printing, Mater. Des. 135 (2017) 26–36, http://dx.doi.org/10.1016/j.matdes.2017.08.069.

[34] Hendrik Thölking, Ferdinand Cerbe, Michael Sinapius, Analytical-numerical simulation of 4D-structures printed with FDM, Mater. Today: Proc. 101 (2024) 15–21, http://dx.doi.org/10.1016/j.matpr.2023.02.040.

[35] William Antonio Pancho Ramirez, Rafiq Ahmad, Cagri Ayranci, Influence of 4D printing parameters on the stored pre-strain of flat structures fabricated with polyurethane-based shape memory polymer (SMPU), Prog. Addit. Manuf. 10 (9) (2025) 6673–6690, http://dx.doi.org/10.1007/s40964-025-00999-5.

[36] Xuguang Xu, Huilin Ren, Shengyang Chen, Xiaofan Luo, Feihu Zhao, Yi Xiong, Review on melt flow simulations for thermoplastics and their fiber reinforced composites in fused deposition modeling, J. Manuf. Process. 92 (2023) 272–286.

[37] Saeed Behseresht, Young Ho Park, Allen Love, Omar Alejandro Valdez Pastrana, Application of numerical modeling and finite element analysis in fused filament fabrication: A review, Materials 17 (17) (2024) 4185.

[38] Marcin P. Serdeczny, Raphaël Comminal, David B. Pedersen, Jon Spangenberg, Experimental validation of a numerical model for the strand shape in material extrusion additive manufacturing, Addit. Manuf. 24 (2018) 145–153, http://dx.doi.org/10.1016/j.addma.2018.09.022.

[39] Andreas Lendlein, Marc Behl (Eds.), Shape-memory polymers, in: Advances in Polymer Science, vol. 226, Springer, Berlin and Heidelberg, 2010, http://dx.doi.org/10.1007/978-3-642-12359-7.

[40] Fabian Neumann, Ferdinand Cerbe, Michael Sinapius, From material to solution: Implementing shape memory behavior of thermoplastic polymers in commercial FEA software for structural analysis, J. Manuf. Mater. Process. 9 (3) (2025) 73, http://dx.doi.org/10.3390/jmmp9030073.

[41] Claire McIlroy, Peter D. Olmsted, Deformation of an amorphous polymer during the fused-filament-fabrication method for additive manufacturing, J. Rheol. 61 (2) (2017) 379–397, http://dx.doi.org/10.1122/1.4976839.

[42] Marcin P. Serdeczny, Raphaël Comminal, Md. Tusher Mollah, David B. Pedersen, Jon Spangenberg, Numerical modeling of the polymer flow through the hot-end in filament-based material extrusion additive manufacturing, Addit. Manuf. 36 (2020) 101454, http://dx.doi.org/10.1016/j.addma.2020.101454.

[43] Eliana M. Agaliotis, Baltazar D. Ake-Concha, Alejandro May-Pat, Juan P. Morales-Arias, Celina Bernal, Alex Valadez-Gonzalez, Pedro J. Herrera-Franco, Gwénaëlle Proust, J. Francisco Koh-Dzul, Jose G. Carrillo, Emmanuel A. Flores-Johnson, Tensile behavior of 3D printed polylactic acid (PLA) based composites reinforced with natural fiber, Polymers 14 (19) (2022) http://dx.doi.org/10.3390/polym14193976.

[44] Claire McIlroy, Peter. D. Olmsted, Disentanglement effects on welding behaviour of polymer melts during the fused-filament-fabrication method for additive manufacturing, Polymer 123 (2017) 376–391, http://dx.doi.org/10.1016/j.polymer.2017.06.051.

[45] Raphaël Comminal, Marcin P Serdeczny, David B Pedersen, Jon Spangenberg, Numerical modeling of the strand deposition flow in extrusion-based additive manufacturing, Addit. Manuf. 20 (2018) 68–76, http://dx.doi.org/10.1016/j.addma.2017.12.013.

[46] Jun Liu, Kelly L. Anderson, N. Sridhar, Direct simulation of polymer fused deposition modeling (fdm)—an implementation of the multi-phase viscoelastic solver in OpenFOAM, Int. J. Comput. Methods 17 (01) (2020) 1844002.

[47] Behrouz Behdani, Matthew Senter, Leah Mason, Ming Leu, Joontaek Park, Numerical study on the temperature-dependent viscosity effect on the strand shape in extrusion-based additive manufacturing, J. Manuf. Mater. Process. 4 (2) (2020) http://dx.doi.org/10.3390/jmmp4020046.

[48] Emily R Fitzharris, Narumi Watanabe, David W Rosen, Meisha L Shofner, Effects of material properties on warpage in fused deposition modeling parts, Int. J. Adv. Manuf. Technol. 95 (5) (2018) 2059–2070, http://dx.doi.org/10.1007/s00170-017-1340-8.

[49] Mehul Lukhi, Christoph Mittermeier, Josef Kiendl, Multi-physics simulation of a material extrusion-based additive manufacturing process: towards understanding stress formation in the printed strand, Prog. Addit. Manuf. 10 (9) (2025) 6839–6853, http://dx.doi.org/10.1007/s40964-025-01012-9.

[50] Felipe A. González, Stefanie Elgeti, Marek Behr, Ferdinando Auricchio, A deforming-mesh finite-element approach applied to the large-translation and free-surface scenario of fused deposition modeling, Internat. J. Numer. Methods Fluids 95 (2) (2023) 334–351, http://dx.doi.org/10.1002/fld.5151.

[51] Felipe A. González, Boundary-conforming Finite-Element Methods Applied to Fused Deposition Modeling (Ph.D. thesis), RWTH Aachen University, 2023, http://dx.doi.org/10.18154/RWTH-2023-07148, Dissertation, RWTH Aachen University, 2023.

[52] Felipe A. González, Stefanie Elgeti, Marek Behr, The surface-reconstruction virtual-region mesh update method for problems with topology changes, Internat. J. Numer. Methods Engrg. 124 (9) (2023) 2050–2067, http://dx.doi.org/10.1002/nme.7200.

[53] Marcin P. Serdeczny, Raphaël Comminal, David B. Pedersen, Jon Spangenberg, Numerical simulations of the mesostructure formation in material extrusion additive manufacturing, Addit. Manuf. 28 (2019) 419–429, http://dx.doi.org/10.1016/j.addma.2019.05.024.

[54] Sina Jafarzadeh, Raphaël Comminal, Marcin P. Serdeczny, Mohamad Bayat, Christian RH Bahl, Jon Spangenberg, Geometric characterization of orthogonally printed layers in material extrusion additive manufacturing: numerical modeling and experiments, Prog. Addit. Manuf. 8 (6) (2023) 1619–1630.

[55] Huanxiong Xia, Jiacai Lu, Sadegh Dabiri, Gretar Tryggvason, Fully resolved numerical simulations of fused deposition modeling. part I: fluid flow, Rapid Prototyp. J. 24 (2) (2018) 463–476, http://dx.doi.org/10.1108/RPJ-12-2016-0217.

[56] Huanxiong Xia, Jiacai Lu, Gretar Tryggvason, A numerical study of the effect of viscoelastic stresses in fused filament fabrication, Comput. Methods Appl. Mech. Engrg. 346 (2019) 242–259, http://dx.doi.org/10.1016/j.cma.2018.11.031.

[57] Huanxiong Xia, Jiacai Lu, Gretar Tryggvason, Simulations of fused filament fabrication using a front tracking method, Int. J. Heat Mass Transfer 138 (2019) 1310–1319, http://dx.doi.org/10.1016/j.ijheatmasstransfer.2019.04.132.

[58] Zhenyu Ouyang, Erwan Bertevas, Di Wang, Boo Cheong Khoo, Julien Férec, Gilles Ausias, Nhan Phan-Thien, A smoothed particle hydrodynamics study of a non-isothermal and thermally anisotropic fused deposition modeling process for a fiber-filled composite, Phys. Fluids 32 (5) (2020).

[59] Anne Gosset, David Barreiro-Villaverde, Juan Carlos Becerra Permuy, Marcos Lema, Ana Ares-Pernas, María José Abad López, Experimental and numerical investigation of the extrusion and deposition process of a poly (lactic acid) strand with fused deposition modeling, Polymers 12 (12) (2020) 2885, http://dx.doi.org/10.3390/polym12122885.

[60] Easir Arafat Papon, Anwarul Haque, Muhammad Ali Rob Sharif, Numerical study for the improvement of bead spreading architecture with modified nozzle geometries in additive manufacturing of polymers, Rapid Prototyp. J. 27 (3) (2021) 518–529.

[61] Sun Kyoung Kim, David O. Kazmer, Non-isothermal non-Newtonian three-dimensional flow simulation of fused filament fabrication, Addit. Manuf. 55 (2022) 102833.
[62] David Xu, Jean F. Agassant, Franck Pigeonneau, Dimensions of the deposited strand in the material extrusion process: Experimental and numerical investigations, Addit. Manuf. 59 (2022) 103107.
[63] Mengyuan Zhou, Liang Si, Peng Chen, Maoyuan Li, Yun Zhang, Huamin Zhou, Dequn Li, Experimental investigation and numerical simulations of temperature and morphology in material extrusion additive manufacturing, Int. J. Adv. Manuf. Technol. 119 (7) (2022) 4863–4876, http://dx.doi.org/10.1007/s00170-022-08663-w.
[64] Xiaohui Ao, Shengxiang Lin, Jianhua Liu, Huanxiong Xia, Junfeng Meng, Modeling and self-supporting printing simulation of fuse filament fabrication, Sci. Rep. 14 (1) (2024) 16275.
[65] Junfeng Meng, Jianhua Liu, Huanxiong Xia, Xiaohui Ao, Wang Zhang, A reduced-order model of thermo-viscoelastic filaments in a material extrusion process, Addit. Manuf. 91 (2024) 104343.
[66] Neda Stoehr, Benjamin Baudrit, Peter Heidemeyer, Martin Bastian, PLA unter der rheologischen lupe, Kunststoffe (2) (2015) 81–84.
[67] Marnix van Gurp, Jo Palmen, Time-temperature superposition for polymer blends, Rheol. Bull. 67 (1) (1998) 5–8.
[68] W.P. Cox, E.H. Merz, Correlation of dynamic and steady flow viscosities, J. Polym. Sci. 28 (118) (1958) 619–622, http://dx.doi.org/10.1002/pol.1958.1202811812.
[69] Francesco Lambiase, Francesco Pace, Elena Andreucci, Alfonso Paoletti, The effect of the interlayer time and deposition speed on the tensile properties of material extrusion components, Int. J. Adv. Manuf. Technol. 133 (11–12) (2024) 6111–6121, http://dx.doi.org/10.1007/s00170-024-14111-8.
[70] Yousef Saad, ILUT: A dual threshold incomplete LU factorization, Numer. Linear Algebra Appl. 1 (4) (1994) 387–402, http://dx.doi.org/10.1002/nla.1680010405.
[71] Andrew A. Johnson, Tayfun Tezduyar, Mesh update strategies in parallel finite element computations of flow problems with moving boundaries and interfaces, Comput. Methods Appl. Mech. Engrg. 119 (1–2) (1994) 73–94, http://dx.doi.org/10.1016/0045-7825(94)00077-8.
[72] Patrick J. Roache, Verification and Validation in Computational Science and Engineering, Hermosa Publishers, 1998.
[73] S.F. Costa, F.M. Duarte, J.A. Covas, Thermal conditions affecting heat transfer in FDM/FFE: a contribution towards the numerical modelling of the process, Virtual Phys. Prototyp. 10 (1) (2015) 35–46, http://dx.doi.org/10.1080/17452759.2014.984042.
[74] Xunfei Zhou, Sheng-Jen Hsieh, Thermal analysis of fused deposition modeling process using infrared thermography imaging and finite element modeling, in: Thermosense: Thermal Infrared Applications XXXIX, vol. 10214, SPIE, 2017, pp. 51–64.
[75] S.F. Costa, F.M. Duarte, J.A. Covas, Estimation of filament temperature and adhesion development in fused deposition techniques, J. Mater. Process. Technol. 245 (2017) 167–179.
[76] Pietro Rando, Marco Ramaioli, Numerical simulations of sintering coupled with heat transfer and application to 3D printing, Addit. Manuf. 50 (2022) 102567, http://dx.doi.org/10.1016/j.addma.2021.102567.